Noname manuscript No.
(will be inserted by the editor)

Progress, challenges, and perspectives of the 3D MHD numerical modeling of oscillations in the solar corona

Leon Ofman

Received: date / Accepted: date

Abstract Recent high temporal and spatial resolution satellite observations of the solar corona provide ample evidence of oscillations in coronal structures. The observed waves and oscillations can be used as a diagnostic tool of the poorly known coronal parameters, such as magnetic field, density, and temperature. The emerging field of coronal seismology relies on the interpretation of the various coronal oscillations in terms of theoretically known wave modes, and the comparison of observed and theoretical wave mode properties for the determination of the coronal parameters. However, due to complexity of coronal structures the various modes are coupled, and the application of linear theory of idealized structures to coronal loops and active regions limits the usefulness of such methods. Improved coronal seismology can be achieved by the development of full 3D MHD dynamical model of relevant coronal structures and the oscillation phenomena. In addition to improved accuracy compared to linear analysis, 3D MHD models allow the diagnostic method to include nonlinearity, compressibility, and dissipation. The current progress made with 3D MHD models of waves in the corona are reviewed, the challenges facing further development of this method are discussed in the perspective of future improvement that will be driven by new high resolution and high cadence satellite data, such as received from Hinode and STEREO, and expected from SDO.

Keywords Sun: corona · Magnetic fields · MHD waves · Three-dimensional MHD models · Coronal loops · Coronal active regions · Coronal seismology

L. Ofman
Catholic University of America and
NASA Goddard Space Flight Center
Greenbelt, MD 20771
USA
E-mail: Leon.Ofman@nasa.gov
Also at: Department of Geophysics and Planetary Science,
Tel Aviv University, Tel Aviv, Israel

1 Introduction

The modeling of oscillations in the solar corona is motivated by recent high temporal and spatial resolution of waves in coronal structures by the Solar and Heliospheric Observatory (SOHO), Transition Region and Coronal Explorer (TRACE), Solar-Terrestrial Relations Observatory (STEREO), and Hinode satellites. In the near future high rate data expected from Solar Dynamics Observatory (SDO) will likely contain ample evidence of waves. The observed oscillations can be used as a diagnostic tool of the poorly known coronal parameters, such as magnetic field, density, and temperature that can supplement other remote sensing methods. In addition, waves can play a role in the heating of coronal plasma, and information on dissipation processes can be obtained from the damping of the oscillations, and therefore provide insights on the heating mechanism of the solar corona.

The use of MHD waves for the determination of coronal loop parameters was first discussed by Roberts et al. (1984). Individual loop oscillations provide information on localized density and magnetic field structure. The MHD wave diagnostics of the magnetic field, density and temperature in coronal loops became possible routinely only recently with the launch of SOHO and TRACE satellites leading to numerous studies (e.g. Aschwanden et al. 1999; Nakariakov et al. 1999; Nakariakov and Ofman 2001; Aschwanden et al. 2002; Ofman 2002; De Moortel et al. 2002; Goossens et al. 2002; Aschwanden et al. 2003; Verwichte et al. 2004; Wang and Solanki 2004; Terradas and Ofman 2004; Aschwanden 2005; Taroyan et al. 2005; Andries et al. 2005; Verwichte et al. 2006; Wang et al. 2007; Van Doorsselaere et al. 2007; Ballai 2007; Arregui et al. 2007; Erdélyi and Fedun 2007; Zaqarashvili and Murawski 2007; Verth and Erdélyi 2008; Goossens et al. 2008; McEwan et al. 2008; Jess et al. 2008). Recently launched Hinode satellite and STEREO spacecraft provide additional observations of waves.

This review is focused on 3D MHD modeling of transverse or fast magnetosonic waves. For completeness, we mention that longitudinal waves in coronal loops and plumes were also observed with SOHO spacecraft and TRACE satellite (Ofman et al. 1997; Deforest and Gurman 1998; Ofman et al. 1998; Berghmans and Clette 1999; Ofman et al. 2000; Robbrecht et al. 2001; Ofman and Wang 2002; De Moortel et al. 2002; Kliem et al. 2002; Wang et al. 2002, 2003; King et al. 2003; De Moortel and Hood 2003; De Moortel et al. 2003; McEwan and de Moortel 2006). The waves were interpreted as slow magnetosonic waves (Ofman et al. 1997, 1999; Nakariakov et al. 2000). These waves are seen to be damped on time scale of several tens of minutes, and on typical length scale of several tens of Mm. Since slow magnetosonic waves propagate along the field in low-β corona plasma, they can be modeled usually adequately with one-dimensional codes. The effect of thermal conduction and viscosity on the damping of longitudinal waves in coronal loops and plumes was investigated (e.g. Ofman et al. 2000; Ofman and Wang 2002; De Moortel et al. 2003; Mendoza-Briceño et al. 2004), and it was found that the value of the thermal conduction, and longitudinal (compressive) viscosity is consistent with the theoretically predicted value for coronal plasma. This is in contrast to the case for transverse (shear) viscosity or resistivity, where the theoretically predicted value is too small to account for the observed dissipation of transverse waves (Nakariakov et al. 1999; Ofman and Aschwanden 2002).

Large scale coronal waves were first observed in EUV by the SOHO spacecraft's Extreme ultraviolet Imaging Telescope (EIT) (Thompson et al. 1999). High resolution and cadence (compared to SOHO/EIT) TRACE satellite observations have shown that the waves can induce oscillation in coronal loops (Wills-Davey and Thompson 1999;

Ballai et al. 2005). Recent STEREO twin spacecraft observations allow reconstructing the detailed temporal evolution of the waves in 3D (Veronig et al. 2008; Long et al. 2008; Patsourakos et al. 2009; Gopalswamy et al. 2009). The waves are associated with flares and Coronal Mass Ejections (CMEs) and propagate at typical speeds of 200-500 km/s on the solar disk. These waves are sometimes seen to be associated with Moreton waves (e.g. Warmuth et al. 2001) observed in H α (Moreton 1960), that were interpreted as fast magnetosonic waves by Uchida (1970), who also suggested using the wave properties for diagnosis of coronal magnetic structures. The coronal EIT waves were interpreted as fast MHD waves as well (Wang 2000; Murawski et al. 2001; Ofman and Thompson 2002). Although, other interpretations seems plausible in some cases that appear in the wide spectrum of observations which are categorized as "EIT waves" (e.g. Wills-Davey et al. 2007; Delannée et al. 2008), recent observations by STEREO provide strong support that EIT waves are propagating fast mode waves (Patsourakos et al. 2009; Gopalswamy et al. 2009). Three-dimensional MHD models were used to study EIT waves in several papers (Wu et al. 2001; Ofman and Thompson 2002; Terradas and Ofman 2004; Ofman 2007). The 3D MHD studies support as well the interpretation of EIT waves in terms of fast magnetosonic wave.

Three-dimensional, nonlinear, resistive MHD model of coronal loops as inhomogeneous slabs in Cartesian geometry were studied in the past by Ofman et al. (1994), and (Ofman and Davila 1995, 1996). In particular, Ofman et al. (1994) have shown that Kelvin-Helmholtz instability can develop at the resonance absorption layer boundaries in a coronal loop, resulting in enhanced dissipation. Early attempts were made to model the nonlinear evolution of resonant absorption of Alfvén waves in cylindrical loop model using nonlinear resistive 3D MHD models (Poedts and Goedbloed 1994, 1997). The resistive 3D MHD studies of coronal loops were focused on the heating of coronal loops by the resonant absorption of Alfvén waves, and stability of the resonant absorption layer. In these studies the Alfvén waves were driven continuously by a source inside or outside the loops, and the waves were dissipated by resistivity and viscosity in the resonant layers in the loops.

Recently, the transverse oscillations of cylindrical, and of four-threaded cylindrical loops in Cartesian box were studied using nonlinear, resistive 3D MHD model by Terradas and Ofman (2004), and by Ofman (2005, 2009). In these studies the oscillations were excited by a velocity pulse to model the effect of a flare, a CME, or an impact of an EIT waves on the loops in coronal active regions. Oscillations of loops with more realistic three-dimensional magnetic geometry that are embedded in bipolar magnetic field were carried out by Miyagoshi et al. (2004), and in a potential magnetic dipole by McLaughlin and Ofman (2008), and recently by Selwa and Ofman (2008); Ofman and Selwa (2009). The later studies allow investigating the effect of the surrounding non-uniform magnetic structure and curvature on the trapping, and leakage of wave in curved coronal loops.

Following numerous detailed observational, analytical, and computational studies and the controversies regarding the role of various modes, or the damping mechanisms (see the reviews by Roberts 2000; Nakariakov and Verwichte 2005, and others in this volume) it is now evident that the complexity of the observed oscillations due to fine structure, mode coupling, gravity, nonlinearity, and dissipation requires full (i.e., time-dependent, nonlinear, resistive, with gravity) 3D MHD modeling in order to apply coronal seismology accurately to the variety of oscillations observed in coronal structures. This review highlights recent results of 3D MHD studies.

2 Observational Motivation

Ample evidence for wave activity in the solar corona was obtained since the launch of SOHO and TRACE satellites. In this section, several examples of wave activity observed recently by TRACE, STEREO, and Hinode spacecraft are reviewed. These observations serve as motivation and justification for 3D MHD modeling, and the results of the models can be used for coronal seismology.

In figure 1a the image of the active region AR 8270 taken on 1998 July 14 at 12:54UT by TRACE in 171Å is shown. A flare that occurred in this active region shortly afterward lead to coronal loop oscillations. These oscillations were first described by Aschwanden et al. (1999); Nakariakov et al. (1999), and later lead to numerous other studies. This was the first observation of spatially resolved transverse coronal loop oscillations with damping in EUV, to which coronal seismology was applied (Nakariakov et al. 1999; Nakariakov and Ofman 2001). Later, Aschwanden et al. (2002) and Schrijver et al. (2002) compiled a catalogue of TRACE observations of coronal loop oscillations, and analyzed these events. Other observations have followed (see, e.g. Verwichte et al. 2004; Hudson and Warmuth 2004; De Moortel and Brady 2007; Van Doorsselaere et al. 2007; Wang et al. 2008)

The transverse oscillations of a TRACE loop were first modeled using 1.5 D MHD (Nakariakov et al. 1999; Ofman 2002), following by 3D MHD (Terradas and Ofman 2004; Miyagoshi et al. 2004; Ofman 2005), and later the global oscillation of this active region were investigated with 3D MHD simulations (Ofman 2007). Figure 1b shows the magnetic field lines of this AR calculated from the potential extrapolation of the photospheric field observed by NSO Kitt Peak. The potential field combined with gravitationally stratified density was used as an initial state for the 3D MHD studies (Ofman 2007). Often, potential magnetic field extrapolations are in poor agreement with the observed active region loop structure. However, in this case, there is good overall agreement between the TRACE image and the potential field in most of the active region.

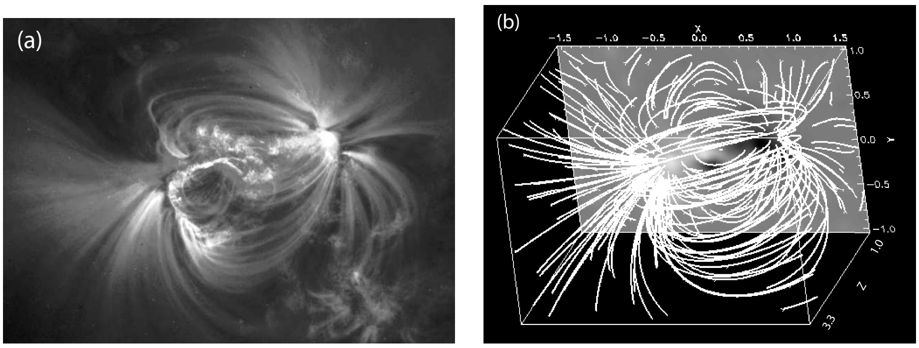

Fig. 1 (a) TRACE 171Å image of AR 8270 taken on 1998 July 14 at 12:54 UT. This image was the last before the impulsive phase of the flare was observed in EUV. (b) Initial magnetic field of the model active region obtained from potential extrapolation of NSO Kitt-Peak photospheric magnetogram. The viewing angle was set to approximate the line of sight of the active region on the Sun (compare to (a)). (adapted from Ofman 2007)

The high resolution (0.1") of Hinode Solar Optical Telescope (SOT) allows resolving the multi-threaded structure of a coronal loop. Although the Hinode/SOT Ca II H line filter is sensitive to chromospheric temperatures, observation of coronal loops is possible, if cooler chromospheric material is contained in coronal loops. This can occur during eruptive events that induce siphon flows in the coronal loops. Ofman and Wang (2008) found the first direct evidence for transverse waves in coronal multi-threaded loops using Hinode/SOT observations on January 12, 2007. The detection of the individual oscillating threads became possible due to the chromospheric material flowing along the threads. Oscillations and flow were seen in multiple threads for about 3 periods (see figure 2), with an average period of 113 ± 2 s. The oscillations were damped on average with a rate of 560±297 s. The thin threads were $\lesssim 0.5''$ wide, and the average speed of the chromospheric material was ~ 100 km s^{-1}. The coronal nature of the loop was confirmed by SOHO EIT observations in 195Å, that showed co-spatial coronal loop.

Ofman and Wang (2008) analyzed the data and concluded that the loops consist of twisted magnetic threads. They found that in some threads, the waves were nearly standing transverse waves with phase speed of 1250 km s^{-1} consistent with fast MHD waves and kink modes, whereas in other threads the waves were propagating fast magnetosonic. Using the properties of the waves and assumptions on density Ofman and Wang (2008) estimated the magnetic field strength in several threads to be 20±7 G. The multi-threaded twisted loops are good candidates for MHD modeling, leading to Gruszecki et al. (2008) 2D MHD study of fast waves in a slab with parallel flow, and Ofman (2009) 3D MHD study of four-threaded twisted oscillating loops (see below).

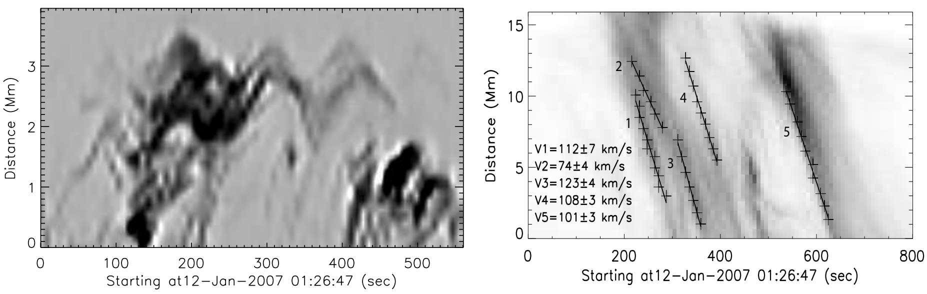

Fig. 2 Time series of the plasma emission in the Ca II H filter in a cut across (left panel) the loop top seen by Hinode/SOT on January 12, 2007 at about 1:30 UT. The right panel shows the flows in the loop in a cut along the loop. The multithreaded structure of the loop is evident (adapted from Ofman and Wang 2008)

In figure 3 two views of an EIT waves from the two STEREO spacecraft (A and B) are shown. The images ware taken in EUV in 171Å using the EUV Imager (EUVI) telescopes on the two spacecraft, and the difference images are shown. The two views allow reconstructing the 3D view of the EIT wave. Using stereoscopic triangulation Patsourakos et al. (2009) found that the height of the wave is about 90Mm above the photosphere, consistent with the height of fast mode wave expected in 1.5MK gravitationally stratified plasma of the quiet sun (see, Patsourakos et al. (2009) for the details of the data analysis). The three-dimensional information contained in this observation makes it a good candidate for 3D MHD modeling.

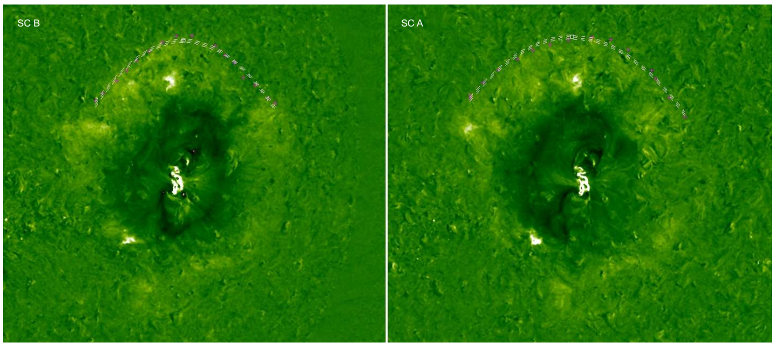

Fig. 3 STEREO/EUVI view of an EIT wave. STEREO spacecraft B (left panel) and STEREO spacecraft A(right panel) images. The two views allow fitting a segment of the wave-front in A+B with a parabola and triangulate the vertexes. The resulting wave height is 90Mm. (adapted from Patsourakos et al. 2009).

3 Three-dimensional MHD Model

3.1 Model Equations

The following normalized, compressive, resistive 3D MHD equations are used to model oscillation in loops and active regions

$$\frac{\partial \rho}{\partial t} + \nabla \cdot (\rho \mathbf{v}) = 0, \tag{1}$$

$$\frac{\partial \mathbf{v}}{\partial t} + (\mathbf{v} \cdot \nabla)\mathbf{v} = -\frac{\beta}{2\rho}\nabla p + \frac{\mathbf{J} \times \mathbf{B}}{\rho} - \frac{1}{F_r r^2}, \tag{2}$$

$$\frac{\partial \mathbf{B}}{\partial t} = \nabla \times (\mathbf{v} \times \mathbf{B}) + \frac{1}{S}\nabla^2 \mathbf{B}, \tag{3}$$

$$\left(\frac{\partial}{\partial t} + \mathbf{v} \cdot \nabla\right) \frac{p}{\rho^\gamma} = (\gamma - 1)(S_h + S_l), \tag{4}$$

where β is the ratio of thermal to magnetic pressure given by $\beta = 2C_s^2/(\gamma V_A^2)$, C_s is the sound speed, and $V_A = B/\sqrt{4\pi\rho}$ is the Alfvén speed, the Lundquist number $S = \tau_A/\tau_r$ is the ratio of the typical Alfvén time ($\tau_A = a/V_A$, where a is the typical lengthscale of the model) to the resistive diffusion time ($\tau_r = 4\pi a^2/\nu c^2$, where ν is the resistivity, and c is the speed of light), the Froude number is $F_r = V_A^2 R_s/(GM_s)$, G is the gravitational constant, M_s is the solar mass, and R_s is the solar radius. In the energy equation S_h is the heating term, and S_l is the loss term (i.e., heat conduction, and radiation). However, in the study of transverse oscillations isothermal plasma is assumed ($\gamma = 1$), and therefore the equation of state is used to calculate the pressure $p = k_b n T_0$, where k_B is Boltzmann's constant.

Note that incompressible MHD equations can not correctly describe the coupling of Alfvénic and compressive modes in coronal loop oscillations, while ideal MHD equations lead to singularities in the solutions for oscillating coronal loops, and therefore, can not provide physical description of resonant absorption of Alfvén waves.

For million degree uniform solar plasma the Lundquist number is believed to be $S = 10^{14}$, based on Spitzer's conductivity. However, due to numerical limitations of the 3D MHD computations typically the value of $S = 10^4$ is used. The lower value of the Lundquist number is consistent with faster evolution of dissipative processes in the coronal plasma than the ideal value of S would imply (e.g. Dere 1996; Nakariakov et al. 1999; Ofman and Aschwanden 2002).

3.2 Boundary, and initial conditions

Here we summarize the boundary and the initial conditions for the two main types of studies reviewed in this paper: individual loops (Terradas and Ofman 2004; Ofman 2005, 2009), and model active regions (Ofman and Thompson 2002; Ofman 2007; McLaughlin and Ofman 2008; Ofman and Selwa 2009).

3.2.1 Straight single loop

The initial state in Cartesian geometry, where the z-coordinate is along the loop, and x-y plane is across the loop radius, consists of a nearly uniform (see figure 4) background magnetic field in the z direction $\mathbf{B}_0(x, y) = B_{0,z}(x, y)\mathbf{e}_z$, and a dense loop defined by

$$\rho_0(x, y, z) = \rho_{\min} + (\rho_{\max} - \rho_{\min})e^{-[(x^2+y^2)/r_0^2]^q}, \tag{5}$$

where $r_0 = 0.5$ is the loop radius, $\rho_{\max}$ is the maximal density inside the loop, and $\rho_{\min}$ is the density outside the loop, and q is used to define the sharpness of the loop boundary (typically we use $q = 2$). Note that in order to maintain pressure balance we require that $B_0^2 + \beta p_0 = const.$ in normalized units across the loop. In the low-β active region this implies that a small decrease (of order β in normalized units) in B_0 inside the loop is needed to maintain pressure balance. The typical computational domain was a Cartesian box of size $L_x \times L_y \times L_z = 6 \times 6 \times 10$ in normalized units. To model longer loops $L_z \approx 15$ was used.

3.2.2 Straight four-threaded loop

For the case of four closely spaced straight cylinders (i.e., the distance between the loops is comparable to the loop radius) the initial density of the loops is given by

$$\rho_0(x, y, z) = \rho_{\min} + (\rho_{\max} - \rho_{\min}) \sum_{i=1}^{4} e^{-\{[(x-x_i)^2+(y-y_i)^2]/r_0^2\}^2}, \tag{6}$$

where $\rho_{\min} = 0.2$ is the minimal normalized density outside the loops, $\rho_{\max} = 1$ is the maximal normalized density of the loops, $r_0 = 0.25$ is the radius of the loops, and (x_i, y_i), where $i = 1, 2, 3, 4$ are the locations of the axis of the four threads in the normalized coordinate system used by Ofman (2007) was: $(-0.5, 2.7, z)$, $(0.5, 2.7, z)$, $(0, 2.2, z)$, $(0, 3.2, z)$.

3.2.3 Loop Boundary conditions

In this section the boundary conditions used by Ofman (2009) are reviewed. The line-tied boundary conditions at $z = z_{\min}$ are given by

$$\mathbf{B}(x, y, z_{\min}, t) = (0, 0, B_0(x, y)), \tag{7}$$

$$\mathbf{V}(x, y, z_{\min}, t) = (0, 0, V_0(x, y)), \tag{8}$$

$$\rho(x, y, z_{\min}, t) = \rho_0(x, y), \tag{9}$$

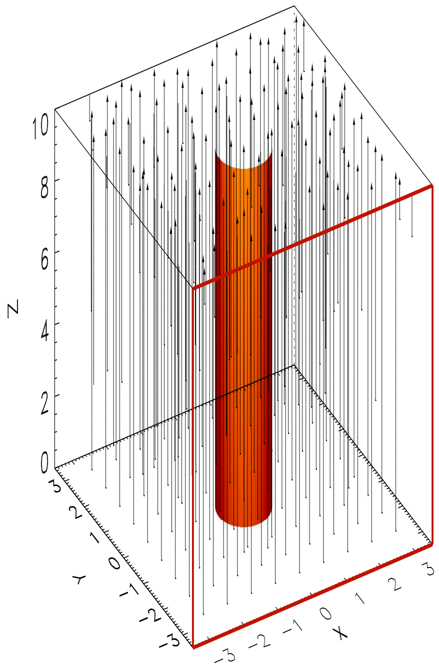

Fig. 4 A model of a single straight cylindrical loop directed along the magnetic field (shown with vectors). The orange square marks the boundary of the velocity pulse. A single isosurface of the loop density is shown. Note that the loop boundary is smoothly varying according to equation (5).

where the normalized magnetic field was $B_0 = 1$ outside the loop, and reduced slightly inside the loop to conserve pressure balance according to $B_0(x,y)^2 + \beta\rho_0(x,y) = const$ in the isothermal plasma. These boundary conditions were applied for parallel threaded loop, and following the application of the twist. The boundary conditions at the other end of the loops ($z = z_{\rm max}$) were line-tied as well. These boundary conditions are consistent with transverse loop oscillations, such that, the location of the loop footpoint is fixed in the boundary plane. When background flow was introduced the boundary condition were modified, allowing outflow at $z = z_{\rm max}$.

At the other four planes open boundary conditions are applied on the variables:

$$\mathbf{B}(x_{min,max}, y, z, t) = \mathbf{B}(x_{min,max} \pm \Delta x, y, z, t), \tag{10}$$
$$\mathbf{V}(x_{min,max}, y, z, t) = \mathbf{V}(x_{min,max} \pm \Delta x, y, z, t), \tag{11}$$
$$\rho(x_{min,max}, y, z, t) = \rho(x_{min,max} \pm \Delta x, y, z, t), \tag{12}$$

where Δx is the grid spacing in the x direction. Similar expressions are used for the boundary conditions at $y_{min,max}$.

At the other four planes open boundary conditions are applied on the variables:

$$\mathbf{B}(x_{min,max}, y, z, t) = \mathbf{B}(x_{min,max} \pm \Delta x, y, z, t), \tag{13}$$
$$\mathbf{V}(x_{min,max}, y, z, t) = \mathbf{V}(x_{min,max} \pm \Delta x, y, z, t), \tag{14}$$

$$\rho(x_{min,max}, y, z, t) = \rho(x_{min,max} \pm \Delta x, y, z, t), \tag{15}$$

where Δx is the grid spacing in the x direction. Similar expressions are used for the boundary conditions at $y_{min,max}$.

To introduce the twist in the four-threaded loop case the following form of the velocity was applied at the boundary at $z = z_{\rm min}$ for a time interval that produced about ninety degree clockwise rotation (below the threshold for kink instability) at the thread axis

$$\mathbf{v}(x, y, z = z_{\rm min}, t) = \omega_t r_c(\cos\,\theta, -\sin\,\theta, 0)e^{-(r_c - r_{c0})/\delta r}, \tag{16}$$

where $\omega_t = 0.1$ is the angular rotation velocity, and we define $r_c = [(x-x_c)^2+(y-y_c)^2]^{\frac{1}{2}}$ as the radial distance from the central axis of the four threads located at $(x_c, y_c) = (0, 2.7)$, and $\theta = \arctan[(x - x_c)/(y - y_c)]$ is the projection angle. The exponential decay function ensures that the rotation velocity is zero far from the loop, where $r_{c0} = 0.75$ and $\delta r = 0.2$. During the application of the rotation at $z = z_{\rm min}$ the magnetic field, density, and vertical velocity were extrapolated from the internal points to the boundary in the z-direction. When the rotation was complete the boundary conditions reverted to line-tied.

3.2.4 Model active region

In this section the boundary conditions used by Ofman and Thompson (2002) and related studies are reviewed. The boundary conditions at z_{min} (coronal base) were given by

$$\mathbf{B}(x, y, z_{min}, t) = \mathbf{B}_0(x, y), \tag{17}$$

$$\mathbf{V}(x, y, z_{min}, t) = 0, \tag{18}$$

$$\rho(x, y, z_{min}, t) = \rho_0, \tag{19}$$

where $\mathbf{B}_0(x, y)$ was the magnetic field obtained from potential extrapolation of the observed photospheric field. In Ofman (2007) the magnetic field of AR8270 from the NSO Kitt-Peak magnetogram was used (see the right panel in figure 1). In that study the size of the computational domain was about $220,000 \times 147,000 \times 162,000$ km in the lower corona. The magnetic field magnitude in the computational domain was normalized by the maximal magnitude (∼370 G) of the extrapolated magnetic field at the base of the corona. For simplicity, constant density of $n_0 = 10^{10}$ cm^{-3} was used as the boundary condition at the base of the active region. The initial density in the computational domain was gravitationally stratified with scale height temperature of $T_0 = 10^6$ K.

At the other five planes open boundary conditions are applied on the variables:

$$\mathbf{B}(x_{min,max}, y, z, t) = \mathbf{B}(x_{min,max} \pm \Delta x, y, z, t), \tag{20}$$

$$\mathbf{V}(x_{min,max}, y, z, t) = \mathbf{V}(x_{min,max} \pm \Delta x, y, z, t), \tag{21}$$

$$\rho(x_{min,max}, y, z, t) = \rho(x_{min,max} \pm \Delta x, y, z, t), \tag{22}$$

where Δx is the grid spacing in the x direction. Similar expressions are used for the boundary conditions at $y_{min,max}$, and at z_{max}.

3.2.5 Model active region with dense loop

In order to investigate the effect of dense loop on the propagation and damping of waves in an active region a dipole field was used as an initial state. First, gravitationally stratified density was introduced throughout the model active region. Next, a single fluxtube was selected, and higher density plasma was introduced inside the fluxtube using equation (5), where the loop radius was varied according to the width of the flux tube in the dipole field (see Figure 14).

3.2.6 Velocity pulse

To excite transverse loop oscillations the initial velocity pulse in the positive x-direction (sideways) was applied at the $y-z$ boundary plane for the duration $\Delta t = 2\tau_A$ given by

$$\mathbf{v}(x_{\min}, y, z, t) = v_p \mathbf{e}_x, \tag{23}$$

where the amplitude of the pulse was $v_p = 0.05V_A$. The pulse parameters were optimized by experimenting with several values of v_p, and Δt, and choosing the values that produce loop oscillation in qualitative agreement with observations. The boundary condition were time dependent at $x = x_{min}$ and changed to open after the pulse has left the computational domain. At $z = z_{min}$ and $z = z_{max}$ the boundary conditions were line-tied. In Ofman (2005) the pulse in equation (23) was multiplied by $\sin(\pi/L_z z)$ to excited the fundamental mode.

For Ofman (2007) model active regions the initial velocity pulse in the positive z-direction (upward) was applied in the region $(-0.6, 0.6) \times (-0.6, 0)$ in $x - y$ plane at the coronal boundary. The region was chosen to approximately coincide with the location of the flare observed in EUV with TRACE. The following boundary condition on the velocity was used:

$$\mathbf{V}(x, y, z_{min}, t) = V(t)\mathbf{e}_z, \tag{24}$$

where $V(t)$ has the following temporal dependence (see figure 5)

$$V(t) = V_0 e^{-\left(\frac{t-t_0}{\Delta t}\right)^8}, \tag{25}$$

where V_0 is the amplitude of the pulse, t_0 is the initial time of the pulse, and $2\Delta t$ is the pulse duration. In Ofman (2007) model $V_0 = 0.012V_A = 96$ km s^{-1}, $t_0 = 15\tau_A$, and $\Delta t = 6.5\tau_A = 57$ s were used. The parameters were optimized by experimenting with several values of V_0, and Δt, and choosing the values that agree best with the TRACE data results.

The velocity pulse propagates in the model active region and through the lower boundary, where density is allowed to adjust self consistently via zero-order extrapolation from the internal computational region. Thus, the density compression associated with the velocity pulse propagates together with the waves. After the pulse has left the computational domain, the boundary condition at $z = z_{min}$ reverts to line-tied.

The initial background density is given by the gravitationally stratified hydrostatic density

$$\rho(r) = \rho_0 e^{\frac{R_s}{H}\left(\frac{R_s}{r}-1\right)}, \tag{26}$$

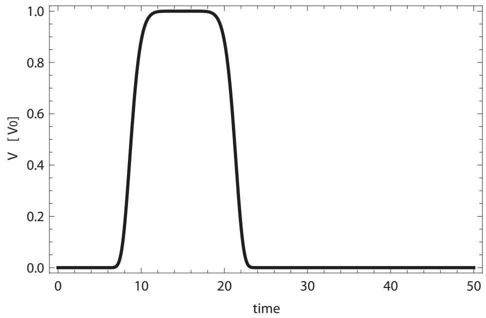

Fig. 5 The typical temporal evolution of the velocity pulse (equation (23)) used to initiate the oscillations in a model active regions (Ofman 2007).

where the normalized gravitational scale height is $H = 2k_B T_0 R_s/(GM_s m_H)$, $m_{\rm H}$ is the hydrogen mass, and r is the heliocentric distance in units of R_s. For small heights in the corona the above expression can be approximated by $\rho(z) \approx \rho_0 e^{-z/H}$. The density is given in units of the base coronal density n_0. The velocity is in units of the Alfvén speed $V_A \approx 8070$ km s^{-1} in Ofman (2007).

4 Overview of Recent Model Results

4.1 Single and Four-threaded Loops

Recently, Terradas and Ofman (2004) demonstrated the use of 3D MHD simulation for the determination of the plasma β in a coronal loop. This is possible when the transverse wave has sufficiently large amplitude to cause nonlinear compression of the density in the loop by the ponderomotive force. In figure 6 (left panel) the maximum relative density perturbation at the apex of the loop is shown as a function of β for two valued of transverse velocity amplitude. The observational point is determined from TRACE observations of the 1998 July 14 flare and the associated loop oscillations. The wave velocity amplitude and the density enhancement were determined from observation. By placing the point on the plot of the parametric study, it was possible to determine the value of $\beta = 0.04 \pm 0.01$ in that loop.

The results of the 3D MHD study by Terradas and Ofman (2004) of the loop compression are shown in the right panel of figure 6. The isosurface of the loop density is shown at two times during the oscillation: $t = 3\tau_A$ (light gray), overlayed with the same density isosurface at $t = 37\tau_A$ (dark gray). The relative enhancement of the loop density in the central part of the loop is evident.

Using the 2.5D MHD of an arcade, and 3D MHD model of a loop in Cartesian geometry Terradas and Ofman (2004) found that large initial Alfvénic disturbances produce a pressure imbalance along the loop, which results in an upflow from its legs that leads to the accumulation of mass at the loop top in the initial stages of the oscillations. At later times, the pressure gradient due to the density enhancement becomes dominant and inhibits further density increase. As seen in figure 6 the results of the numerical study are consistent with observations, and provide new additional tool for coronal seismology.

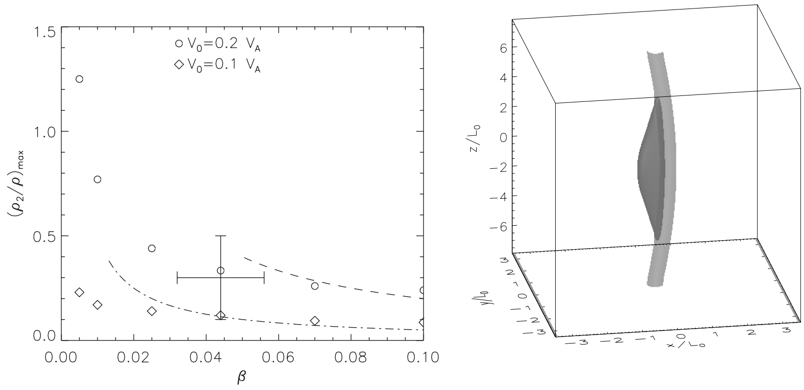

Fig. 6 Left panel: Maximum density perturbation at the apex of the loop as a function of β for two transverse wave velocity amplitudes, $V_0 = 0.1V_A$ (diamonds), $V_0 = 0.2V_A$(circles). The dashed and dot-dashed curves represent the values calculated according to the one-dimensional model (see Terradas and Ofman 2004) for $V_0 = 0.1V_A$ and $V_0 = 0.2V_A$, respectively. The observational point plotted with the error bars was obtained from TRACE 1998 July 14 data shown in figure 1. Right panel: density isosurface ($\rho = 0.95$) at time $t = 3\tau_A$ (light gray), overlayed with the same density isosurface at $t = 37\tau_A$ (dark gray) obtained from the 3D MHD model. For this simulation $V_0 = 0.2V_A$ and $\beta = 2.5 \times 10^{-2}$. Adapted from Terradas and Ofman (2004).

Ofman (2005) used 3D resistive MHD model to compare the damped oscillations of a single loop impacted by an EIT wave to the damped oscillations of a four-threaded loop. The spacing of the threads was comparable to the thread radius (see figure 7). The EIT wave was modeled by the velocity pulse of the form given by equation (23) multiples by a spatial half-wavelength with nodes at the lower and upper boundaries of the simulation region. This was done to excite predominantly the fundamental mode in the loops. Ofman (2005) found that in a single cylindrical loop the damping rate is independent of the Lundquist number as expected for the resonant absorption (e.g. Steinolfson and Davila 1993; Ofman et al. 1994; Ruderman and Roberts 2002). However, the damping time increases with the Lundquist number for the four threaded loop, for low values of resistivity. The damping time scaling with resistivity for four-threaded loop is close the $S^{1/3}$, as expected for phase mixing (e.g. Heyvaerts and Priest 1983; Steinolfson and Davila 1993). When the resistivity is increased beyond a certain threshold, the damping of the oscillations becomes again nearly independent of resistivity (see figure 8). This could be due to the decoupling of the resistive layers at each thread, since their width decreases with resistivity.

Recently, Arregui et al. (2008) investigated the resonant absorption of two closely spaced coronal loops modeled by slabs using more simplified model (linearized, zero-β resistive MHD). They found that the damping rate of the transverse oscillation in a system of two closely spaced loops differs substantially from the damping of a single loop.

Recently, Ofman (2009) developed 3D MHD model of multi-threaded loop in Cartesian geometry. In the model three cases were investigated: four-threaded loop with parallel threads, four-threaded twisted loop, and four threaded loop with parallel flow along the threads. The initial state for the density is shown in figure 9. The twist given

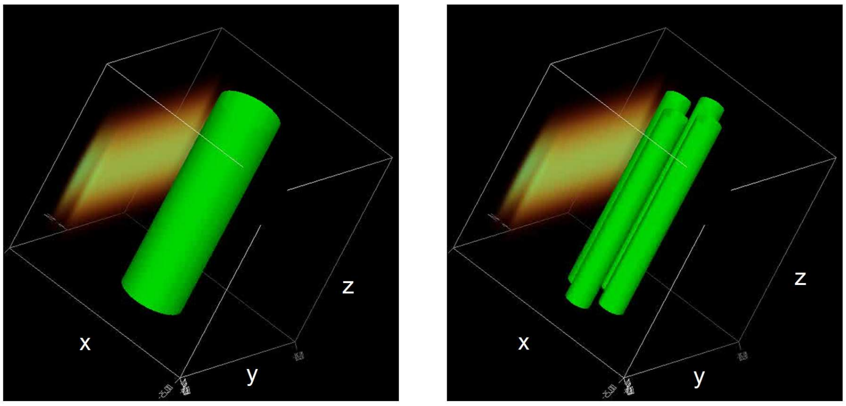

Fig. 7 3D MHD model of active region loops impacted by an EIT wave. The left panel shows an isosurface of a single loop density with the magnetic field in the z direction. The right panel shows density isosurface of four closely spaced loops impacted by the wave. The intensity scale indicates the magnitude of the current density square (J^2) of the impacting wave in arbitrary units. (adapted from Ofman 2005)

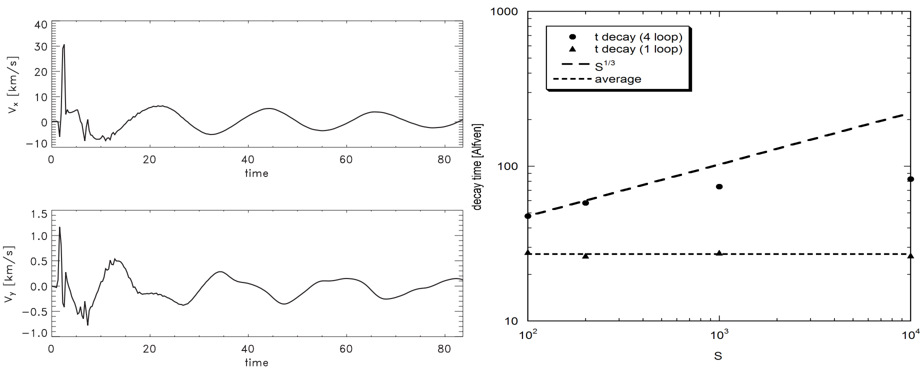

Fig. 8 The typical evolution of the loop velocity following the impact of the EIT wave in the 3D MHD model of Ofman (2005) (left panel). The scaling of the damping time of loop oscillations with the Lundquist number S for a single loop, and for four loops (right panel). The scaling of phase mixing with S is shown with long dashes. The short dashes line indicates the average damping time for a single loop (adapted from Ofman 2005).

by equation (16) was applied at one boundary of the loops, while line-tied boundary condition were used at the other boundary. In order to excite the transverse oscillations the loops were impacted by a velocity pulse given by equation (23).

In figure 10 the temporal evolution of the loop wave velocity and the magnetic field near the center of one loop strand ($V_{z,0}$=0) at (-0.5,2.7,7.90) is shown. When the loop strands are parallel (left panels) the evolution of the oscillations agrees with the expected period of kink-mode for the loop. The damping rate is close to the expected damping rate due to the resonant absorption (Ruderman and Roberts 2002; Ofman 2009). Since the Lundquist number here was $S = 10^4$, the interaction between the parallel threads placed at the distances in this study was weak. However, when twist was applied to the loop, the evolution of the oscillations changes dramatically. The

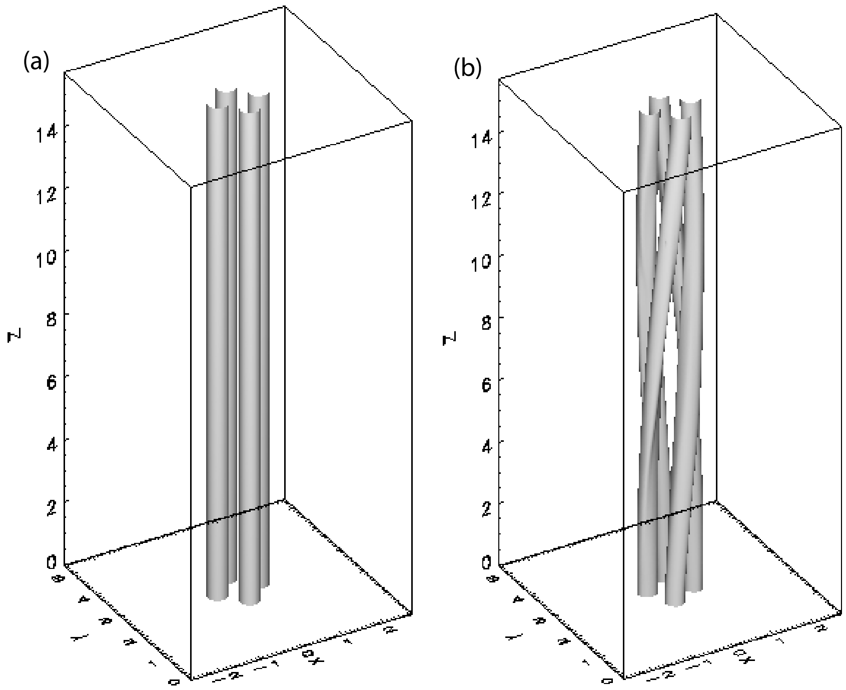

Fig. 9 (a) The density isosurface at $\rho_0 = 0.6$ of the four loops in the initial state. (b) The density isosurface of the four loops following the application of the twist at the lower footpoint (adapted from Ofman 2009). See the animations of the oscillations in the electronic version of Ofman (2009).

period of the oscillations has decreased due to larger effective phase speed of the wave in the twisted loop. Evidently, the damping rate has increased as well, due to the coupling between the velocity components of the four threads introduced by the twist, and increased current dissipation.

In figure 11 the isosurface of the current density j^2 is shown at the beginning of the evolution of the twisted loop, and at $t = 34.2\tau_A$. It is evident that the twisted loop is not current free, and the magnetic configuration is not force-free due to the introduction of the twist. The background currents combine with the currents induced by the impact of the velocity pulse, affecting the oscillations and the damping of the wave. Contrary to the parallel-threaded loop, Ofman (2009) have shown that the complex nonlinear 3D interactions of the twisted four-threaded loop oscillations can not be described well by the kink mode solution of the linearized MHD equations.

Ofman (2009) finds that twisted loop oscillations result in filamented current and velocity structure, and the currents can not be described by the fundamental kink mode solutions of the linearized MHD equations. The twisted loop oscillates and damp faster

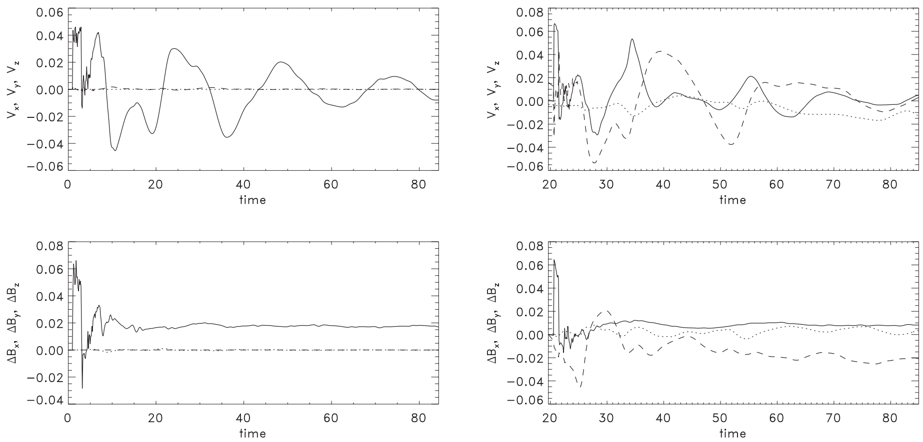

Fig. 10 Temporal evolution of the loop wave velocity and the magnetic field near the center of one loop strand ($V_{z,0}$=0) at (-0.5,2.7,7.90). Left panels show the case without twist, and the right panels show the evolutions of the case with twist. Solid curve corresponds to the x components, dashed curve to the y components, and dotted curve to the z components of the velocity and the magnetic field (adapted from Ofman 2009).

than parallel threaded loop. The results of the study show that internal loop structure, twist, and flow can affect the oscillations and the damping, and therefore must be properly modeled when coronal seismology is applied to observations to coronal loops.

4.2 Model Active Region

Ofman and Thompson (2002) were first to model an active region by an initially force-free, bipolar magnetic configuration with gravitationally stratified plasma using nonlinear, resistive 3D MHD code with gravity. In their model a velocity pulse was launched at the boundary of the region to model the impact of an EIT wave. They showed that the EIT wave is a fast mode wave that undergoes strong reflection and refraction in the active region in agreement with observations showing that EIT waves travel around active regions. Ofman and Thompson (2002) also found that the current-carrying active regions can be destabilized by the impact of an EIT wave, and demonstrated that the interaction between EIT waves and active regions can serve as a diagnostic tool for coronal seismology.

Below is a brief review of the numerical results obtained from the active region model with solar magnetic field developed by (Ofman 2007). The study was motivated by MHD wave activity observed in coronal active region AR 8270 in the extreme ultraviolet (EUV) by TRACE on 1998 July 14. To model the observed wave activity following the flare, a velocity pulse was launched into a model active region from below. The velocity and the density in the $x-y$ plane at $z = 1.47$ of the model active region following the launch of the velocity pulse are shown in figure 12. The velocity pulse was localized and centered at the region of the flare, as seen by TRACE 171Å on July 14, 1998. The intensity scale shows the velocity and the density magnitude, and the arrows show the direction of the flow at times at two times: $t = 22.1$, and $t = 33.1$. It is evident that the wave propagates outward with the local fast magnetosonic speed, in agreement with previous 3D MHD studies (e.g. Wu et al. 2001; Terradas and Ofman

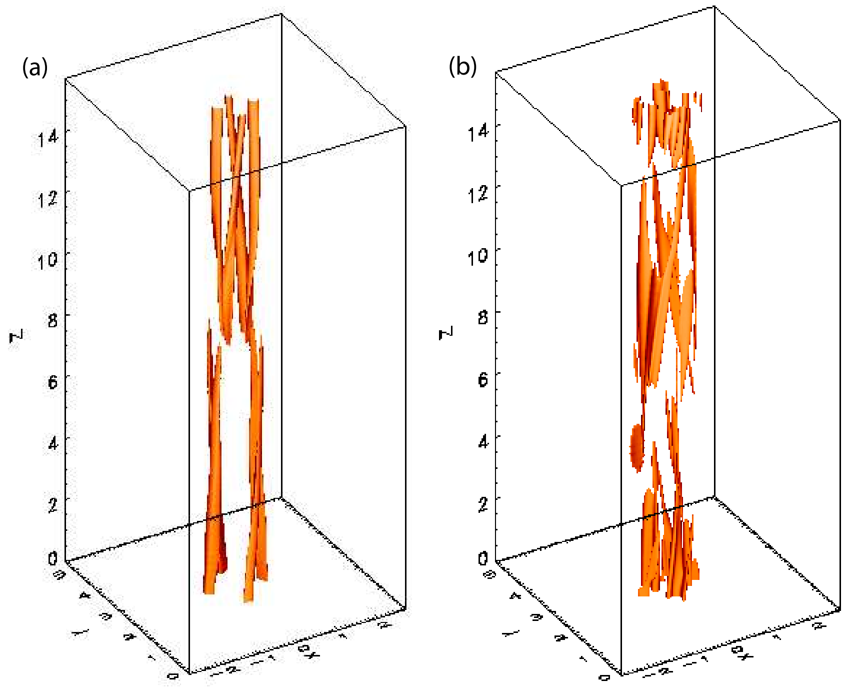

Fig. 11 (a) The current density j^2 isosurface at the level 0.22 for the loops shown in the right panel of figure 9. (b) Same as (a) but at $t = 34.2$ following the impact by the pulse (adapted from Ofman 2009). See the animation of the oscillations in the electronic version of Ofman (2009).

2004; Ofman and Thompson 2002). Thus, the model reproduces the EIT wave launched by the flare and propagating away from the active region.

In figure 13 the temporal evolution of the normalized velocity and the magnetic field components obtained in Ofman (2007) study is shown at two points inside the active region: (0.32,-0.62,1.47), and (0.32,-0.62,1.94). The effects of the propagating fast magnetosonic wave are evident in the initial fluctuations. The oscillations that follow are due to the normal modes of the field line that passes through this point. The oscillations are damped rapidly, since the wave is not trapped, and propagates away from the active region.

Ofman (2007) found that the global oscillations in the model active region are in good qualitative agreement with the oscillations seen in the movies of the TRACE 171Å observations. However, several individual loops in the observations damp on longer timescales compared to the corresponding magnetic field line oscillation damping in the model. This effect was attributed to wave trapping in individual loops in the active region. The wave trapping in individual loops was not modeled in Ofman (2007). Wave

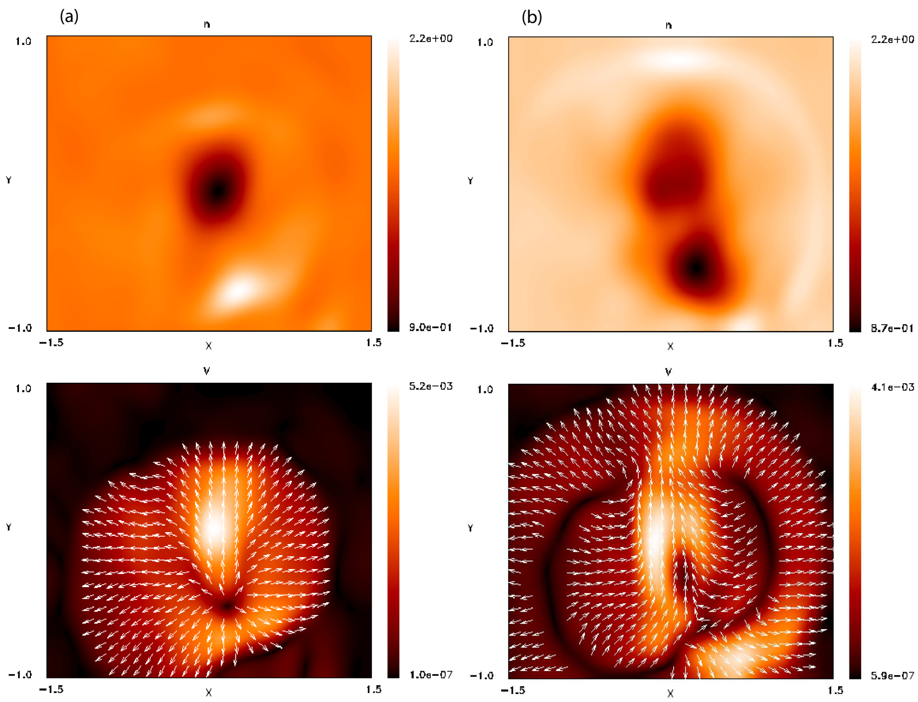

Fig. 12 The velocity and the density in the $x - y$ plane at $z = 1.47$ of the model active region. The intensity scale shows the velocity and the density magnitude, and the arrows show the direction of the flow at times (a) $t = 22.1$, and (b) $t = 33.1$. (adapted from Ofman 2007)

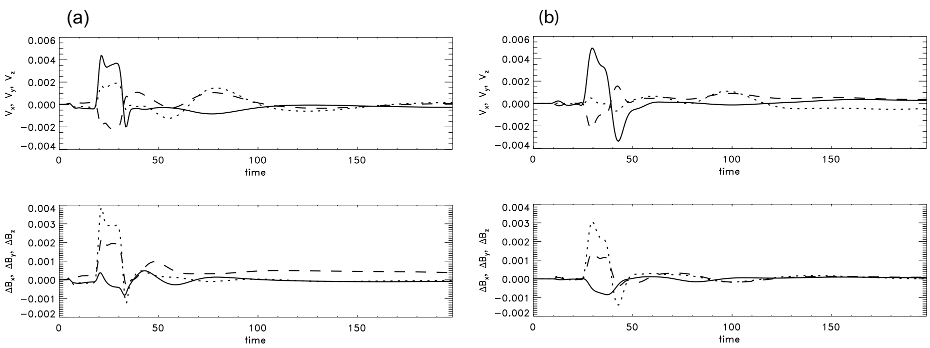

Fig. 13 The temporal evolution of the normalized velocity and the magnetic field at (a) $x = 0.32$, $y = -0.62$, $z = 1.47$, and (b) at $z = 1.94$ due to the velocity pulse launched from below. The z components are shown with solid curves, the y components are shown with dashes, and the x components are shown with dots (adapted from Ofman 2007).

trapping in model active region loops was studied in detail in McLaughlin and Ofman (2008).

4.3 Dense loop in Bi-polar Active Region

In order to investigate the response of a loop to an incoming EIT wave or a pulse in more realistic than slab/cylindrical geometry, a potential bi-polar (Miyagoshi et al. 2004), or a dipole magnetic field (McLaughlin and Ofman 2008; Selwa and Ofman 2008; Ofman and Selwa 2009) were used. The later studies essentially extended Ofman and Thompson (2002) study by including a dense loop in the model bi-polar active region (figure 14). The loop is constructed by adding gravitationally stratified plasma to a given flux tube in the dipole magnetic field, with higher density than the background.

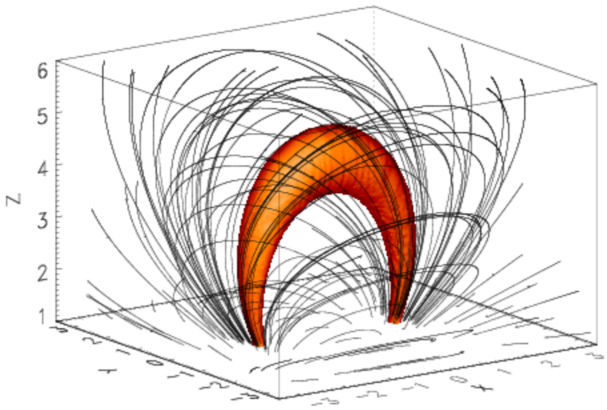

Fig. 14 Initial dipole 3D magnetic field configuration with dense loop shown in color (adapted from Ofman and Selwa 2009).

Miyagoshi et al. (2004) developed 3D MHD model of the transverse oscillations of a coronal loops in a bi-polar potential magnetic field with gravitationally stratified atmosphere. The loop structure included three density regions: corona, transition region, and photosphere. The authors found that the wave period is determined by the loop Alfvén time, and that the oscillations are damped exponentially with time. The authors explained this damping by leakage of fast mode MHD waves out of the loop. In that study damping rate was found to be $\omega_{\rm damp} \propto V_{\rm a}/R$, where $V_{\rm a}$ is the Alfvén speed outside the loop, and R is the radius of the loop. Because of numerical limitations, the plasma was $\beta \geq 0.3$ in Miyagoshi et al. (2004) - much larger than typical coronal values. The authors found that the effect of wave trapping is small for the parameters used in their model.

McLaughlin and Ofman (2008) found that the model EIT wave propagation generates field line oscillations, which are rapidly damped, and that the high density loop can support trapped waves. They found that the impact of the EIT wave excited both horizontal and vertical loop oscillations. They also found that amplitude of the oscillations decreases, and the damping time increases with increasing density contrast. In that model the main damping mechanism was wave leakage due to curvature, since the loop boundary was assumed to be sharp, i.e., it could not support resonant absorption or phase mixing. McLaughlin and Ofman (2008) demonstrated the need for accurate density measurements of individual loops for coronal seismology.

Recently, Ofman and Selwa (2009) investigated the oscillations of a dipole loop, and the effect of the loop density profile across the field on the damping rate of the transverse oscillations induced by a pulse (figure 14-15). The study was motivated by prediction from resonant absorption theory that the damping rate is decreasing with the sharpness of the boundary (Ruderman and Roberts 2002). However, Ofman and Selwa (2009) found that the time signature of the loop oscillations was weakly affected by the sharpness of the loop boundary. This was due to the rapid leakage of the wave out of the loop enhanced by the loop curvature, and the large value of β (compared to typical coronal active region loop value) near the loop apex used in that study (i.e., resonant absorption was not the dominant wave damping mechanism in this model). In this model, β increases rapidly with height, since the gravitationally stratified density and the corresponding thermal pressure decrease exponentially with height, faster than the decrease of magnetic pressure. Currently, a study with lower value of β, more appropriate for typical coronal conditions is under way.

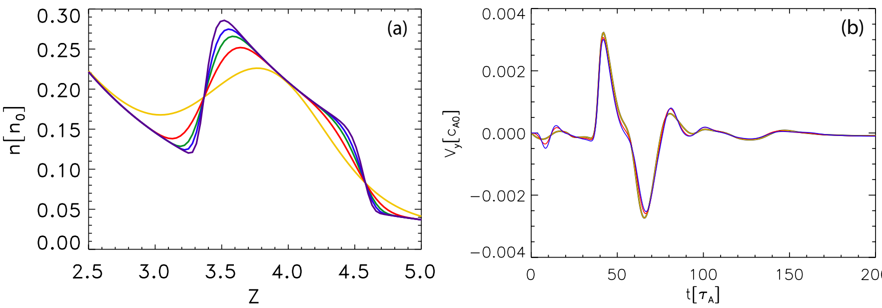

Fig. 15 (a) Various density profiles along z of the loop at $x = y = 0$ (see equation (5): q = 6 (violet line), q = 4 (blue line), q = 3 (green line), q = 2 (red line) and q = 1 (yellow line). (b) Time signatures of the transversal component of velocity that correspond to the loop density profiles shown in (a) (adapted from Ofman and Selwa 2009).

5 Discussion and Conclusions

Recent observations show that coronal loops and active regions are highly structured and exhibit oscillations on time scales of minutes to hours. Impulsively excited wave activity is observed in active regions and in individual loops in EUV, and as Doppler shift oscillations. The periodicity of the waves is determined by the phase speed of the particular mode, and the size of the structure. In some cases the dominant mode can be clearly determined. However, in general it has proven to be difficult to determine the exact phase speed of the observed wave, since it is determined by several factors, such as fine structure, and mode coupling, that are difficult to determine observationally due to limitations of present day instruments.

Regardless of the difficulties, it has been demonstrated in a number of studies that wave activity can be used to study the physical properties of loops and active regions via coronal seismology, i.e., using the observed wave properties to determine poorly known quantities such as $\mathbf{B}$, n, and T by comparing the observed wave period, wavelength, and/or speed to the theoretically expected value in a particular structure. In this review several recent observations of waves were highlighted, and the results of recent 3D MHD studies of waves in coronal loops and in active regions with applications to coronal seismology were reviewed.

The observation and modeling of the waves can also help understanding the heating and stability of coronal active regions and loops. By investigating the damping of the waves, the dissipation coefficients in the coronal plasma could be estimated, if the damping is primarily due to dissipative process, such as viscosity, resistivity or thermal conduction. It has been demonstrated by Ofman and Thompson (2002) that 3D MHD models of active regions can show the onset of instability in non-potential model active region, destabilized by an impulsive event. Due to lack of sufficient observational detail, and due to the difficulty of modeling dissipative processes in the solar corona (where the dissipation coefficients are assumed to be small, with dissipation times orders of magnitude larger than Alfvén transit times), the determination of the dissipation coefficients is challenging and controversial, in particular for transverse waves, and was discussed in several studies (Nakariakov et al. 1999; Ofman and Aschwanden 2002). The dissipation of longitudinal waves is easier to model, due to the much larger dissipation coefficients parallel to the magnetic field (Braginskii 1965), compared to the transverse ones.

Three-dimensional MHD models of active regions with solar boundary conditions have been recently developed to study waves in active regions excited by impulsive events, such as flares, CME's, and the impact of incoming EIT wave generated elsewhere. Improved observations that provide information on three-dimensional active region structure as well as on the propagation of EIT waves in the 3D corona from STEREO require 3D MHD modeling. High spatial and temporal resolution from Hinode/SOT, and spectral information from Hinode/EIS, combined with improved 3D MHD models increase the accuracy of coronal seismology as coronal diagnostic tool, and require detailed modeling that includes individual loops in realistic active region magnetic topology, as well as the internal structure of loops that can dramatically affect the evolution and the damping of the waves, compared to analytical predictions from linearized straight cylinder or slab models.

The new observations, and the future high rate data from SDO requires the development of wave diagnostic tool based on 3D MHD models. This tool, under development today, must be able to incorporate in the near future observational constraints such as realistic magnetic field and loop geometry, and fine structure, and provide rapidly the results of wave modeling, that can be used for coronal seismology in near real-time. These computational requirements, and the necessary level of detail are computationally intensive today, and the relevant models must be parallelized (usually using message passing interface (MPI)) to run on parallel computers, and contain modules for adaptive mesh refinement (AMR) to resolve the fine structure.

Acknowledgements The author thanks the members of the workshop on "Coronal Waves and Oscillations" that was held in International Space Science Institute (ISSI), Bern, Switzerland, in March 2007, and August 2008 for fruitful discussions that lead to this review, and Drs. Spiros Patsourakos, Tongjiang Wang, Małgorzata Selwa for their input. The author also thanks ISSI for their support and hospitality. This work was supported by NASA grants NNG06GI55G, NNX08AV88G, NNX08AP88G, and by NRL grant N00173-06-1-G033.

References

J. Andries, M. Goossens, J.V. Hollweg, I. Arregui, T. Van Doorsselaere, Astron. Astrophys. **430**, 1109–1118 (2005). doi:10.1051/0004-6361:20041832

I. Arregui, J. Andries, T. van Doorsselaere, M. Goossens, S. Poedts, Astron. Astrophys. **463**, 333–338 (2007). doi:10.1051/0004-6361:20065863

I. Arregui, J. Terradas, R. Oliver, J. Luis Ballester, Astrophys. J. **674**, 1179–1190 (2008). doi:10.1086/524934

M.J. Aschwanden, *Physics of the Solar Corona. An Introduction with Problems and Solutions (2nd edition)* (Springer, Chichester, UK; New York, NY, 2005)

M.J. Aschwanden, L. Fletcher, C.J. Schrijver, D. Alexander, Astrophys. J. **520**, 880–894 (1999)

M.J. Aschwanden, B. De Pontieu, C.J. Schrijver, A.M. Title, Solar Phys. **206**, 99–132 (2002)

M.J. Aschwanden, R.W. Nightingale, J. Andries, M. Goossens, T. Van Doorsselaere, Astrophys. J. **598**, 1375–1386 (2003)

I. Ballai, Solar Phys., 72 (2007). doi:10.1007/s11207-007-0415-3

I. Ballai, R. Erdélyi, B. Pintér, Astrophys. J. Lett. **633**, 145–148 (2005). doi:10.1086/498447

D. Berghmans, F. Clette, Solar Phys. **186**, 207–229 (1999)

S.I. Braginskii, in *Review of Plasma Physics* (Consultants Bureau, New York, NY, 1965), pp. 205–311

I. De Moortel, C.S. Brady, Astrophys. J. **664**, 1210–1213 (2007). doi:10.1086/518830

I. De Moortel, A.W. Hood, Astron. Astrophys. **408**, 755–765 (2003)

I. De Moortel, A.W. Hood, J. Ireland, Astron. Astrophys. **381**, 311–323 (2002). doi:10.1051/0004-6361:20011659

I. De Moortel, C.E. Parnell, A.W. Hood, Solar Phys. **215**, 69–86 (2003)

C.E. Deforest, J.B. Gurman, Astrophys. J. **501**, 217–220 (1998)

C. Delannée, T. Török, G. Aulanier, J.F. Hochedez, Solar Phys. **247**, 123–150 (2008). doi:10.1007/s11207-007-9085-4

K.P. Dere, Astrophys. J. **472**, 864 (1996). doi:10.1086/178116

R. Erdélyi, V. Fedun, Science **318**, 1572 (2007). doi:10.1126/science.1153006

M. Goossens, J. Andries, M.J. Aschwanden, Astron. Astrophys. **394**, 39–42 (2002). doi:10.1051/0004-6361:20021378

M. Goossens, I. Arregui, J.L. Ballester, T.J. Wang, Astron. Astrophys. **484**, 851–857 (2008). doi:10.1051/0004-6361:200809728

N. Gopalswamy, S. Yashiro, M. Temmer, J.M. Davila, W.T. Thompson, S. Jones, R.T.J. McAteer, J.P. Wuelser, S. Freeland, R.A. Howard, Astrophys. J. Lett. **691**, 123–127 (2009). doi:10.1088/0004-637X/691/2/L123

M. Gruszecki, K. Murawski, L. Ofman, Astron. Astrophys. **488**, 757–761 (2008). doi:10.1051/0004-6361:200809873

J. Heyvaerts, E.R. Priest, Astron. Astrophys. **117**, 220–234 (1983)

H.S. Hudson, A. Warmuth, Astrophys. J. Lett. **614**, 85–88 (2004). doi:10.1086/425314

D.B. Jess, D.M. Rabin, R.J. Thomas, J.W. Brosius, M. Mathioudakis, F.P. Keenan, Astrophys. J. **682**, 1363–1369 (2008). doi:10.1086/589231

D.B. King, V.M. Nakariakov, E.E. Deluca, L. Golub, K.G. McClements, Astron. Astrophys. **404**, 1–4 (2003). doi:10.1051/0004-6361:20030763

B. Kliem, I.E. Dammasch, W. Curdt, K. Wilhelm, Astrophys. J. Lett. **568**, 61–65 (2002). doi:10.1086/340136

D.M. Long, P.T. Gallagher, R.T.J. McAteer, D.S. Bloomfield, Astrophys. J. Lett. **680**, 81–84 (2008). doi:10.1086/589742

M.P. McEwan, I. de Moortel, Astron. Astrophys. **448**, 763–770 (2006). doi:10.1051/0004-6361:20054041

M.P. McEwan, A.J. Díaz, B. Roberts, Astron. Astrophys. **481**, 819–825 (2008). doi:10.1051/0004-6361:20078016

J.A. McLaughlin, L. Ofman, Astrophys. J. **682**, 1338–1350 (2008). doi:10.1086/588799

C.A. Mendoza-Briceño, R. Erdélyi, L.D.G. Sigalotti, Astrophys. J. **605**, 493–502 (2004). doi:10.1086/382182

T. Miyagoshi, T. Yokoyama, M. Shimojo, Publ. Astron. Soc. Jpn. **56**, 207–214 (2004)

G.E. Moreton, Astron. J. **65**, 494 (1960). doi:10.1086/108346

K. Murawski, V.M. Nakariakov, E.N. Pelinovsky, Astron. Astrophys. **366**, 306–310 (2001). doi:10.1051/0004-6361:20000027

V.M. Nakariakov, L. Ofman, Astron. Astrophys. **372**, 53–56 (2001)

V.M. Nakariakov, E. Verwichte, Living Reviews in Solar Physics **2**, 3 (2005)
V.M. Nakariakov, L. Ofman, E. DeLuca, B. Roberts, J.M. Davila, Science **285**, 862–864 (1999)
V.M. Nakariakov, E. Verwichte, D. Berghmans, E. Robbrecht, Astron. Astrophys. **362**, 1151–1157 (2000)
L. Ofman, Astrophys. J. Lett. **568**, 135–138 (2002). doi:10.1086/340329
L. Ofman, Space Science Reviews **120**, 67–94 (2005). doi:10.1007/s11214-005-5098-1
L. Ofman, Astrophys. J. **655**, 1134–1141 (2007). doi:10.1086/510012
L. Ofman, Astrophys. J. **694**(in press) (2009)
L. Ofman, M.J. Aschwanden, Astrophys. J. **576**, 153–156 (2002)
L. Ofman, J.M. Davila, J. Geophys. Res. **100**, 23427–23442 (1995)
L. Ofman, J.M. Davila, Astrophys. J. Lett. **456**, 123 (1996). doi:10.1086/309875
L. Ofman, M. Selwa, in *IAU Symposium 257: Universal Heliophysical Processes*, ed. by A. Nindos, etal. (Cambridge University Press, New York, NY, 2009)
L. Ofman, B.J. Thompson, Astrophys. J. **574**, 440–452 (2002). doi:10.1086/340924
L. Ofman, T.J. Wang, Astrophys. J. Lett. **580**, 85–88 (2002)
L. Ofman, T.J. Wang, Astron. Astrophys. **482**, 9–12 (2008). doi:10.1051/0004-6361:20079340
L. Ofman, J.M. Davila, R.S. Steinolfson, Astrophys. J. **421**, 360–371 (1994). doi:10.1086/173654
L. Ofman, V.M. Nakariakov, C.E. Deforest, Astrophys. J. **514**, 441–447 (1999)
L. Ofman, V.M. Nakariakov, N. Sehgal, Astrophys. J. **533**, 1071–1083 (2000)
L. Ofman, M. Romoli, G. Poletto, G. Noci, J.L. Kohl, Astrophys. J. **491**, 111–114 (1997)
L. Ofman, M. Romoli, G. Poletto, G. Noci, J.L. Kohl, Astrophys. J. Lett. **507**, 189–189 (1998)
L. Ofman, M. Romoli, G. Poletto, G. Noci, J.L. Kohl, Astrophys. J. **529**, 592–598 (2000)
S. Patsourakos, A. Vourlidas, Y.M. Wang, G. Stanborg, A. Thernisien, Solar Phys., submitted (2009)
S. Poedts, J.P. Goedbloed, Space Science Reviews **68**, 103–108 (1994). doi:10.1007/BF00749123
S. Poedts, J.P. Goedbloed, Astron. Astrophys. **321**, 935–944 (1997)
E. Robbrecht, E. Verwichte, D. Berghmans, J.F. Hochedez, S. Poedts, V.M. Nakariakov, Astron. Astrophys. **370**, 591–601 (2001)
B. Roberts, Solar Phys. **193**, 139–152 (2000)
B. Roberts, P.M. Edwin, A.O. Benz, Astrophys. J. **279**, 857–865 (1984). doi:10.1086/161956
M.S. Ruderman, B. Roberts, Astrophys. J. **577**, 475–486 (2002)
C.J. Schrijver, M.J. Aschwanden, A.M. Title, Solar Phys. **206**, 69–98 (2002)
M. Selwa, L. Ofman, in *First Results From Hinode*, ed. by S.A. Matthews, J.M. Davis, L.K. Harra, Astronomical Society of the Pacific Conference Series, vol. 397, 2008, p. 189
R.S. Steinolfson, J.M. Davila, Astrophys. J. **415**, 354–363 (1993). doi:10.1086/173169
Y. Taroyan, R. Erdélyi, J.G. Doyle, S.J. Bradshaw, Astron. Astrophys. **438**, 713–720 (2005). doi:10.1051/0004-6361:20052794
J. Terradas, L. Ofman, in *ESA SP-547: SOHO 13 Waves, Oscillations and Small-Scale Transients Events in the Solar Atmosphere: Joint View from SOHO and TRACE*, ed. by H. Lacoste, 2004, pp. 469–472
J. Terradas, L. Ofman, Astrophys. J. **610**, 523–531 (2004). doi:10.1086/421514
B.J. Thompson, J.B. Gurman, W.M. Neupert, J.S. Newmark, J.P. Delaboudinière, O.C. St. Cyr, S. Stezelberger, K.P. Dere, R.A. Howard, D.J. Michels, Astrophys. J. Lett. **517**, 151–154 (1999). doi:10.1086/312030
Y. Uchida, Publ. Astron. Soc. Jpn. **22**, 341 (1970)
T. Van Doorsselaere, V.M. Nakariakov, E. Verwichte, Astron. Astrophys. **473**, 959–966 (2007). doi:10.1051/0004-6361:20077783
A.M. Veronig, M. Temmer, B. Vršnak, Astrophys. J. Lett. **681**, 113–116 (2008). doi:10.1086/590493
G. Verth, R. Erdélyi, Astron. Astrophys. **486**, 1015–1022 (2008). doi:10.1051/0004-6361:200809626
E. Verwichte, C. Foullon, V.M. Nakariakov, Astron. Astrophys. **452**, 615–622 (2006). doi:10.1051/0004-6361:20054437
E. Verwichte, V.M. Nakariakov, L. Ofman, E.E. Deluca, Solar Phys. **223**, 77–94 (2004). doi:10.1007/s11207-004-0807-6
T.J. Wang, S.K. Solanki, Astron. Astrophys. **421**, 33–36 (2004). doi:10.1051/0004-6361:20040186
T.J. Wang, D.E. Innes, J. Qiu, Astrophys. J. **656**, 598–609 (2007). doi:10.1086/510424

T.J. Wang, S.K. Solanki, M. Selwa, Astron. Astrophys. **489**, 1307–1317 (2008). doi:10.1051/0004-6361:200810230
T.J. Wang, S.K. Solanki, W. Curdt, D.E. Innes, I.E. Dammasch, Astrophys. J. Lett. **574**, 101–104 (2002). doi:10.1086/342189
T.J. Wang, S.K. Solanki, D.E. Innes, W. Curdt, E. Marsch, Astron. Astrophys. **402**, 17–20 (2003). doi:10.1051/0004-6361:20030448
Y.M. Wang, Astrophys. J. Lett. **543**, 89–93 (2000). doi:10.1086/318178
A. Warmuth, B. Vršnak, H. Aurass, A. Hanslmeier, Astrophys. J. Lett. **560**, 105–109 (2001). doi:10.1086/324055
M.J. Wills-Davey, B.J. Thompson, Solar Phys. **190**, 467–483 (1999)
M.J. Wills-Davey, C.E. DeForest, J.O. Stenflo, Astrophys. J. **664**, 556–562 (2007). doi:10.1086/519013
S.T. Wu, H. Zheng, S. Wang, B.J. Thompson, S.P. Plunkett, X.P. Zhao, M. Dryer, J. Geophys. Res. **106**, 25089–25102 (2001). doi:10.1029/2000JA000447
T.V. Zaqarashvili, K. Murawski, Astron. Astrophys. **470**, 353–357 (2007). doi:10.1051/0004-6361:20077246